Biomimetic artificial water channel membranes for enhanced desalination

Biomimetic artificial water channels membranes for enhanced desalination

Maria Di Vincenzo,[1] Alberto Tiraferri,[2] Valentina-Elena Musteata,[3] Stefan Chisca,[3] Rachid Sougrat,[4] Li-Bo Huang,[1,5] Suzana P. Nunes,[3] Mihail Barboiu[1,5]

[1]Institut Européen des Membranes, Adaptive Supramolecular, Nanosystems Group, University of Montpellier, ENSCM, CNRS, Place Eugène Bataillon, CC 047, F-34095, Montpellier, France. [2] Department of Environment, Land and Infrastructure Engineering (DIATI), Politecnico di Torino, Corso Duca degli Abruzzi 24, 10129 Turin, Italy. [3]King Abdullah University of Science and Technology (KAUST), Biological and Environmental Science and Engineering Division, Advanced Membranes and Porous Materials Center, 23955-6900, Thuwal, SaudiArabia. [4]King Abdullah University of Science and Technology (KAUST), Core Labs, 23955-6900, Thuwal, Saudi Arabia [5]Lehn Institute of Functional Materials, School of Chemistry, Sun Yat-Sen University, Guangzhou 510275, China.

*Corresponding Author. E-mail: mihail-dumitru.barboiu@umontpellier.fr

Biological protein channels in natural membranes utilize highly selective pores to provide exceptional transport performances, in magnitudes far above those achieved by synthetic membranes used for desalination and water treatment. Inspired by biological models, artificial water channels can be used to overcome the permeability/selectivity trade-off of traditional desalination membranes. We demonstrate that the rational incorporation of I–quartet artificial water channels in composite polyamide membranes synthesized *via* interfacial polymerization, provides the first example of biomimetic membranes, applied under representative reverse osmosis desalination conditions, with intrinsically high water-to-salt permeability ratio. The hybrid polyamide network presents larger voids and seamlessly incorporates crystalline assemblies containing I–quartet water channels for highly selective transport of water, while effectively rejecting ions or molecules to enable Å-scale separations. The best biomimetic composite membranes, which can be easily scaled for industrial standards (> m^2), provide remarkable 99.5% rejection of NaCl with water flux of 75 L m^{-2} h^{-1} at 65 bar applied pressure with a 35000 ppm NaCl feed solution at pH 8, representative of seawater desalination. This flux is more than 75% higher than that observed with current state-of-the-art membranes with equivalent solute rejection, translating into an equivalent reduction of the membrane effective area for the same water output and a ~12% reduction of the required energy for

desalination.

Water scarcity is one of the most important challenges of our time[1,2]. Membrane-based technologies have a tremendous role in addressing this challenge by allowing efficient water purification and desalination[3]. Desalination membranes allowing the transport of water while rejecting solutes are used in seawater reverse osmosis (SWRO) and brackish water reverse osmosis (BWRO).

Thin-film composite (TFC) polyamide (PA) membranes prepared *via* interfacial polymerization (IP), have served as standard materials for SWRO and BWRO during the last 40 years[4]. The control of the film thickness and roughness,[5-7] or the incorporation of porous nanofillers[8–10] have been shown to increase the water permeability, while generally leading to lower selectivity, as the resulting defects in the active membrane layer affect the solute retention rate. Fundamentally, to overcome the selectivity-permeance trade-off whilst keeping a water permeance of at least 2-4 L $m^{-2}\,h^{-1}bar^{-1}$[11], completely new approaches would be required.

Biological water channels, the Aquaporins-AQPs[12], exhibit high water permeability and virtually total ionic rejection. The correlated water-protein H-bonding within the 2.8-Å constrained AQP pores stabilize a water superstructure that prevents its disruption and explain the salts/proton exclusion[13]. AQPs have been embedded in artificial *bio-assisted membranes* to enhance the water permeance. Nonetheless, there are many challenges to overcome with the goal to preserve the protein activity at high salinity and high-pressure conditions, or to obtain high-density AQP-based membranes[14]. Parallel to these investigations, straightforward *biomimetic* synthetic approaches to create *artificial water channels*-AWC have been proposed[15,16]. The development of AWCs[17–20] and carbon nanotube porins[21] have increased the prospect to use these materials in desalination technologies, since their structure can be tuned to control the water translocation in a biomimetic fashion[22]. The precisely designed channels are ideal to create membranes with near-perfect selectivity[23]. Centimeter scale flat-sheet polymeric films embedding graphene or/and carbon nanotubes[24-26] or pillar[5]arene channels[27] have led to large improvements in water permeance (20-

65 L $m^{-2}h^{-1}bar^{-1}$), but the salt rejection of these films is typically limited with little interest for seawater desalination. These results are related to important challenges in translating molecular transport to performant meter-scale membranes, thus filtration modules needed for effective desalination. We postulate that one of the creative strategies for addressing such scale-up challenges and to achieve improved performances, in terms of both permeability and selectivity, is to combine the PA material, known for its scalability *via* the integration within a typical roll-to-roll processing system, with the highly permeable and selective AWCs. The key challenge in the construction of such hybrid material is the required adaptive interaction between polyamide chains and water channels, preventing the formation of defects.

Herein, we report the incorporation of AWC within a PA matrix, resulting in the production of scalable biomimetic membranes that remarkably outperform the classical RO membranes. The novel strategy leads to a greater fundamental understanding of how AWC incorporation, starting from their colloidal self-assembled superstructures, can be optimized at the nanoscale to facilitate the selective transport of water, mainly occurring through channels. One novelty here is related to the identification of unexpected sponge-like superstructures of the hybrid PA-AWC materials. Moreover, all other selective channels or materials previously reported in literature[23–27] remain applicable in principle, while the biomimetic membranes reported here are the first materials of this type tested and applied under seawater desalination conditions with representative pressure and crossflow conditions of full-scale systems.

The relatively straightforward quantification of biomimetic imidazole-quartet, I-quartet AWCs, relevant to subsequently construct RO membranes in larger scale based on such probes, is a particularly important and previously unreported strategy.

Kinetic formation of biomimetic AWC embedded membranes prepared via IP. Our fabrication strategy of AWC-PA layers is adding one simple preliminary step to the conventional IP[4] method (Fig. 1a): Hexylureido-imidazole (HC6) were dissolved (1.5 w/w%) in a ethanol/water (85/15 v/v

%), followed by sonication to obtain a colloidal solution of AWC aggregates. This solution was poured onto the active surface of commercial polysulfone (PSf) support before starting the traditional IP procedure. During the IP, the AWCs can produce highly dispersed crystalline phases, that are probably cross-linked with growing PA oligomers into hybrid nanoparticles of 30-40 nm in diameter, integrated into the PA film after a controlled aggregation / crystallization process. The morphology and performance of the final layer depend on the density of the self-assembled I-quartet nanoparticles and on their interaction with the surrounding PA matrix. To improve the performance and the homogeneity the AWCs distribution, different IP protocols were investigated. In the best procedure, the I-quartet solution was left to sit on the PSf for 60 s and a 2 w/w% solution of MPD monomer was made to react with a 0.1 w/w% solution of TMC monomer during the ensuing IP; the membranes thus formed are referred to as "optimized TFC-HC6 membranes". The reference TFC membranes were prepared with the same procedure by contacting them with ethanol, before the IP procedure. To gain insight into the mechanism of formation of AWC colloidal aggregates, we also monitored different samples by dynamic light scattering (DLS). When 0.2 mL of water were added to a 1-mL ethanolic solution of 0.5 % HC6, a reversible formation of aggregates (D_h =600 - 800 nm) was observed, which was followed by a re-dispersion *via* ultra-sonication for 15 min. (Supplementary Fig. 2a). Small angle X-ray scattering (SAXS) profiles provided information on a lower size scale and confirmed that, no structures smaller than 150 nm were detected for diluted HC6 (Supplementary Fig. 3). For more concentrated solutions of 1.0-2.0 % HC6, smaller aggregates (D_h = 70 - 200 nm) were observed after adding 2-6 mL water to 1 mL HC6 ethanolic solution, without any visible precipitation (Supplementary Fig. 2b,c). More interestingly, smaller aggregates (D_h = 70 nm) were obtained when a 2 w/w% aqueous solution of MPD was used instead of pure water (D_h = 200 nm), reminiscent of H-bonding between colloidal aggregates of AWC and MPD (Supplementary Table 1). Additional SAXS experiments performed on samples of 1% HC6 in 5:1 ethanol/water, upon addition of water to shift the ratio to 1:1 indicate

the presence of mass-fractal structures with about 15 nm radius of gyration and Porod slope around 3 (Supplementary Table 2, Fig. 4). These conditions simulate those corresponding to the best results for the nanoaggregates formation and IP membrane preparation in this study.

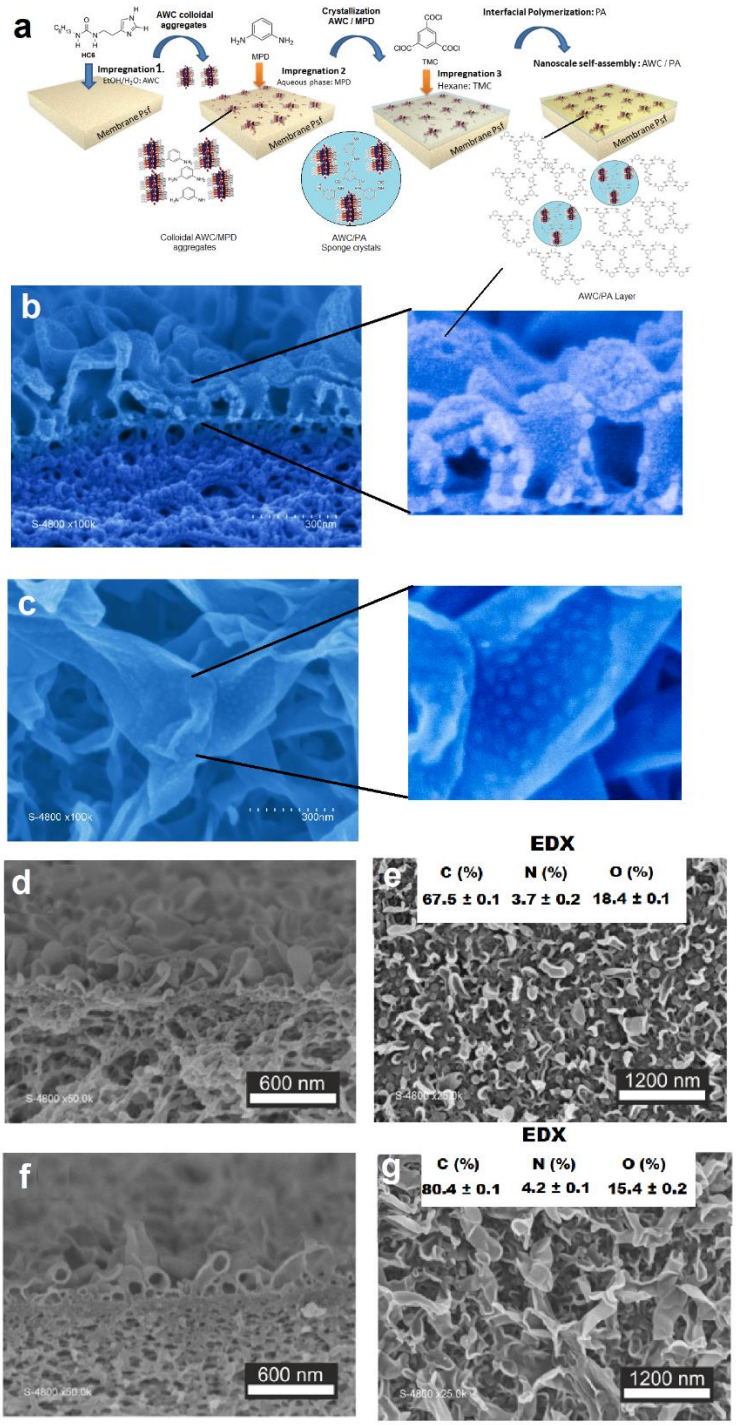

Fig. 1 | Membrane preparation and Scanning Electron Microscopy (SEM) characterization; **(a)** synthetic procedure to obtain the biomimetic TFC-HC6 membrane: impregnation 1 of the PSf ultrafiltration support with an aqueous/ethanolic solution of HC6, followed by the impregnation 2 with an aqueous solution of m-phenylenediamine (MPD) monomer and then the impregnation 3

with a hexane solution of trimesoyl chloride (TMC) monomer to begin to the IP and obtain the composite polyamide (PA) TFC-HC6 membranes incorporating AWCs. Representative SEM micrographs of **(b)** cross-sectional and **(c)** top view of the uppermost layer of TFC-HC6 films. SEM micrographs of **(d, f)** (left) cross-sectional and **(e,g)** of the surface showing compact structures of control TFC membranes **(d,e)** and the formation of large voids at the psf/PA interface of TFC-HC6 membranes **(f,g).** The elemental analysis was performed for each membrane by using energy dispersive X-ray spectroscopy (EDX).

To better explain the kinetics of the of hybrid AWC-PA particles formation and integration into PA, it is important first to consider their spontaneous nano-crystallization from water/ethanol solutions. The X-ray powder diffraction patterns of bulk crystalline powders obtained from colloidal suspensions are indicative of lamellar phases, with the main diffraction peaks at 2θ = 3.46° (*100*), 6.95° (*200*), and 8.04° (*300*), corresponding to interplanar distances of 25.4, 12.5, and 8.4 Å, respectively[20,22], and of the two contracted polymorphs (2θ = 3.62° or 4.09° (*100*)), representing up to 10 % of the weight of the specimen (Supplementary Fig. 6). The match between the distances of the ordered rows observed in the TEM micrograph and the periodicity of parallel sheets of the alternative I-quartets in X-ray single crystal structure, indicates that the nanoparticles obtained from colloidal solutions have a crystalline layered arrangement. We hypothesize that this phenomenon occurs in the first step of membrane synthesis, when the HC6 solution is poured on the surface of the PSf support. Subsequently, the IP procedure entails the contact of the support with an aqueous solution of MPD and aggregated phases of AWC/MPD are formed. Specifically, a heterogeneous nucleation is promoted by H-bonding between MPD and nano-aggregated colloidal AWC, as shown by DLS analysis, while no a massive crystallization process was observed, suggesting that this colloidal solution is present inside the support and does not form an solid interlayer, as previously observed for other solid CNTS, GO, or MOFs fillers[28]. In the final IP step, the membrane is immersed in the TMC hexane phase, where the IP between MPD and TMC occurs roughly 10 seconds at the organic phase side of the interface. In this step, the diffusion of the pre-formed AWC/MPD colloids to the organic phase is disfavored, compared with the diffusion of MPD molecules, but they may interact with growing PA segments *via* H-bonding. This process results in the formation of cross-linked hybrid AWC-PA nanoparticles. They are embedded into the incipient

PA layer formed on top and surrounding the nanoparticles. The new type of hybrid material is therefore generated *via* a nucleation/IP mechanism, supported by experimental results reported here. Scanning electronic microscopy (SEM) images of the TFC-HC6 membrane show the presence of the sponge like nanoparticles, incorporated within the PA layer of TFC-HC6 membranes (Fig. 1b,c), while they are not observed for pristine membrane TFC. The close inspection of the SEM cross-sections and membrane surfaces (Fig. 1e,g) reveals a ridge-and-valley surface morphology typical of IP[28-31]. However, the features observed with the incorporation of AWC are clearly larger than those of the pristine TFC membrane (Fig. 2d,e). This is also confirmed by atomic force microscopy (AFM) results (Supplementary Fig. 5).

The TEM microscopy confirmed that, compared to reference pristine TFC layers (Fig. 2a), which have an homogeneous thickness of ~250 nm, the TFC-HC6 layers (Fig. 2b) have alternated thinner layers (~250 nm) alternate and thicker (~500 nm) regions, a morphology that might also contribute to a higher surface area and therefore, higher permeance. It is also clear that we have a more complex internal structure when the AWC are added, with differentiated domains in the TFC-HC6 layers. The AWC/PA nanoparticles, corresponding to the internal brighter spots are clearly observed by TEM (Fig S7b-d), have diameter ~20-40 nm and are homogeneously enclosed (30-40 spots/100 μm^2) within the PA matrix (Fig. 2b). The PA layer was preferentially stained with OsO_4 or RuO_4, to improve the contrast of the PA regions, that appears darker/grey in the regular cross-sectional TEM images of TFC (Fig. 2a) and TFC-HC6 membranes (Fig. 2b). These areas are also clearly visible in the RuO_4 stained 2D TEM (Supplementary Fig.7) and TEM tomography (Supplementary Fig. 8) images. In the TFC-HC6 membranes, the heavy Os or Ru elements with high electron density, particularly stain the PA layer and are distributed around the brighter spots (Fig. 2b, detail) with a lower electron density. The presence of AWC inside the membrane is corroborated by results obtained with attenuated total reflectance (ATR)- Fourier transform infrared (FTIR) (Supplementary Figure 9) and energy dispersive X-ray (EDX) (Fig. 1e,g, Supplementary

Table 3) spectroscopies: a) in addition to the vibrational bands of the PA matrix present in the TFC membrane, FTIR spectra of TFC-HC6 contain the -CH_2-,as and -CH_2-,sym stretches of the alkyl chains in the range 2750 – 2957 cm^{-1}, as well as urea-NHC=O and imidazole stretches at 1612 cm^{-1} and 1579 cm^{-1}, suggesting the incorporation of the HC6; b) the sharp band at 3300 cm^{-1} attributed to the O-H stretching vibration of strongly H-bonded water within I-quartet channels became much broader, due to the presence of relaxed and mobile water within the hybrid TFC-HC6 membrane; c) the elemental composition determined by EDX varied when AWC were incorporated in the PA, exhibiting a trend with up to 10-12% higher fraction of % C for TFC-HC6 layers and a concurrent reduction mainly in % O.

The complexity of the structure can be more clearly seen in the 3D TEM tomography movies (Supplementary Figure 8) or as screen shots of the 100-nm slices of the samples while tilting them at different angles (Fig. 2c), showing that larger voids and bright spots can be observed inside the TFC-HC6 when compared with the pristine TFC micrographs (Supplementary Fig. 7a and 8a), where very few or no bright spots are seen. The PSf support has much less contrast, appearing as light gray areas in the regular TEM (below the yellow line in Fig. 2a), while the PA layer formed on the surface of the PSf porous support is clearly darker. In the tomography in Fig. 2d, the position of the interface between the PSf support and the formed PA layer (green in Fig. 2d) is represented by a dash line. The less dense white grey spots that are hypothesized to be mostly composed by AWC/PA nanoparticles are marked purple in Fig. 2d. The relative volume occupied by the bright (purple in Fig. 2d) spots was estimated to be 20% by conducting the segmentation and calculating the total voxel of the purple zones relative to the total volume occupied by the complete PA/AWC layer.

Desalination performance: proof of concept, chemical and mechanical stability under RO conditions. The nanostructural distribution of sponge-like PA-AWC regions within the TFC films are essential to control their performance, since they determine the pathways for the water flow

across the active film (Fig. 2e,f). For the first time, biomimetic membranes were tested under high-pressure crossflow conditions, representative of seawater desalination operations in real plants. Specifically, optimized TFC-HC6 active layers comprising AWC provided a consistent increase in water flux of roughly 75% and 150% in the desalination of mimicked seawater (Fig. 3a) and brackish water (Fig. 3d), respectively, compared to lab-made control TFC membranes.

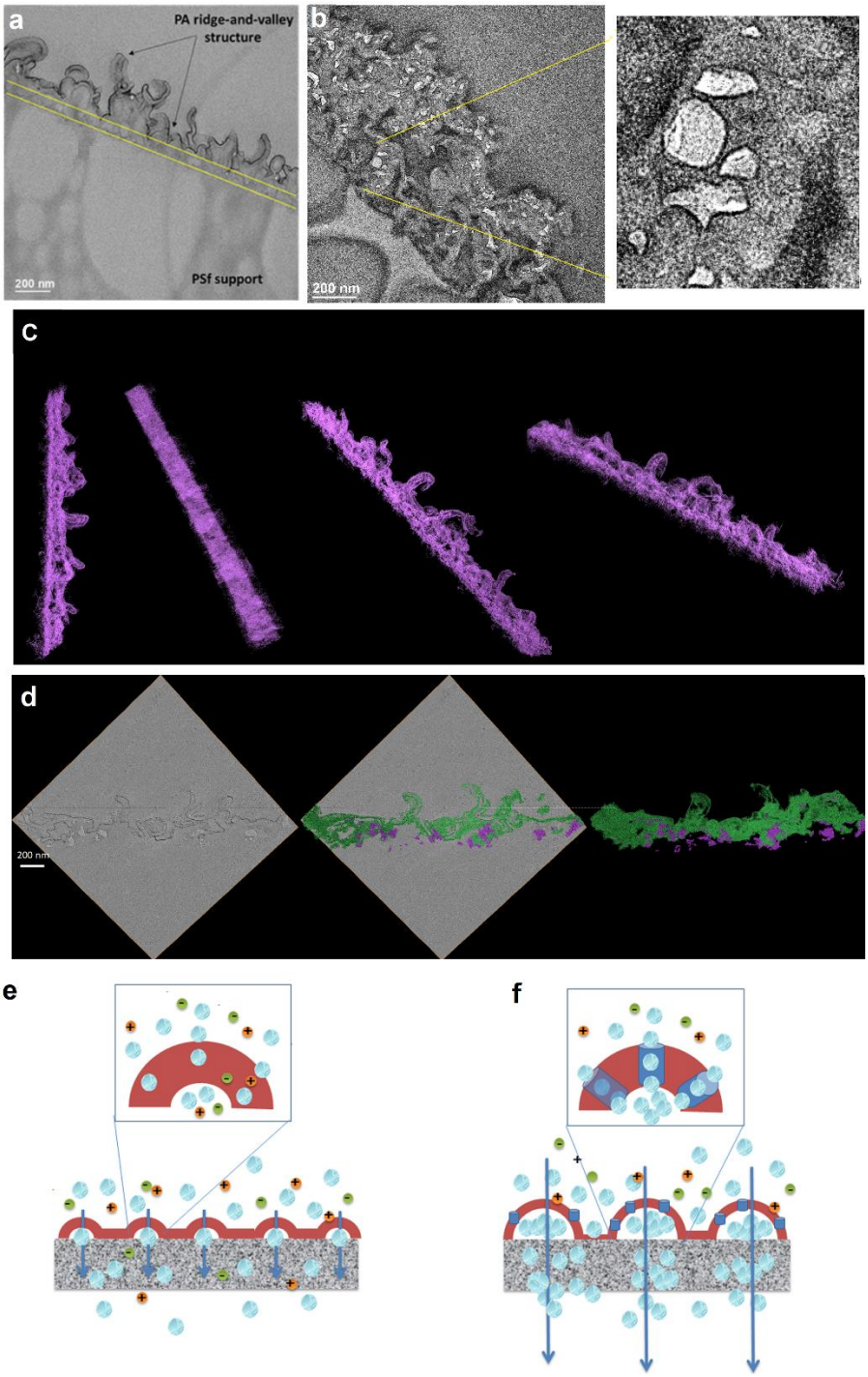

Fig. 2 | Morphological TEM characterization of the membranes. TEM cross-sectional images of **(a)** the pristine PA on porous PSf support and **(b)** detail of the top layer of the TFC-HC6 membrane with high magnification (membranes stained with OsO_4). **(c)** 3D reconstruction TEM tomography of TFC-HC6 membrane in different tilting angles. **(d)** Instantaneous screen shots of TFC-HC6 membrane tomography at a fixed angle: the PA layer formed on the surface of the PSf porous support (not visible) is marked in green. The less dense grey brighter spots, which could correspond to the AWC/PA nanoparticles are marked purple and represent an occupied relative volume of 20%. Schematic representation of the selective transport of water (blue spheres) *versus* ions (green and red spheres) across **(e)** compact pristine TFC and (**f**) AWC-embedded TFC-HC6 membranes with larger surface area.

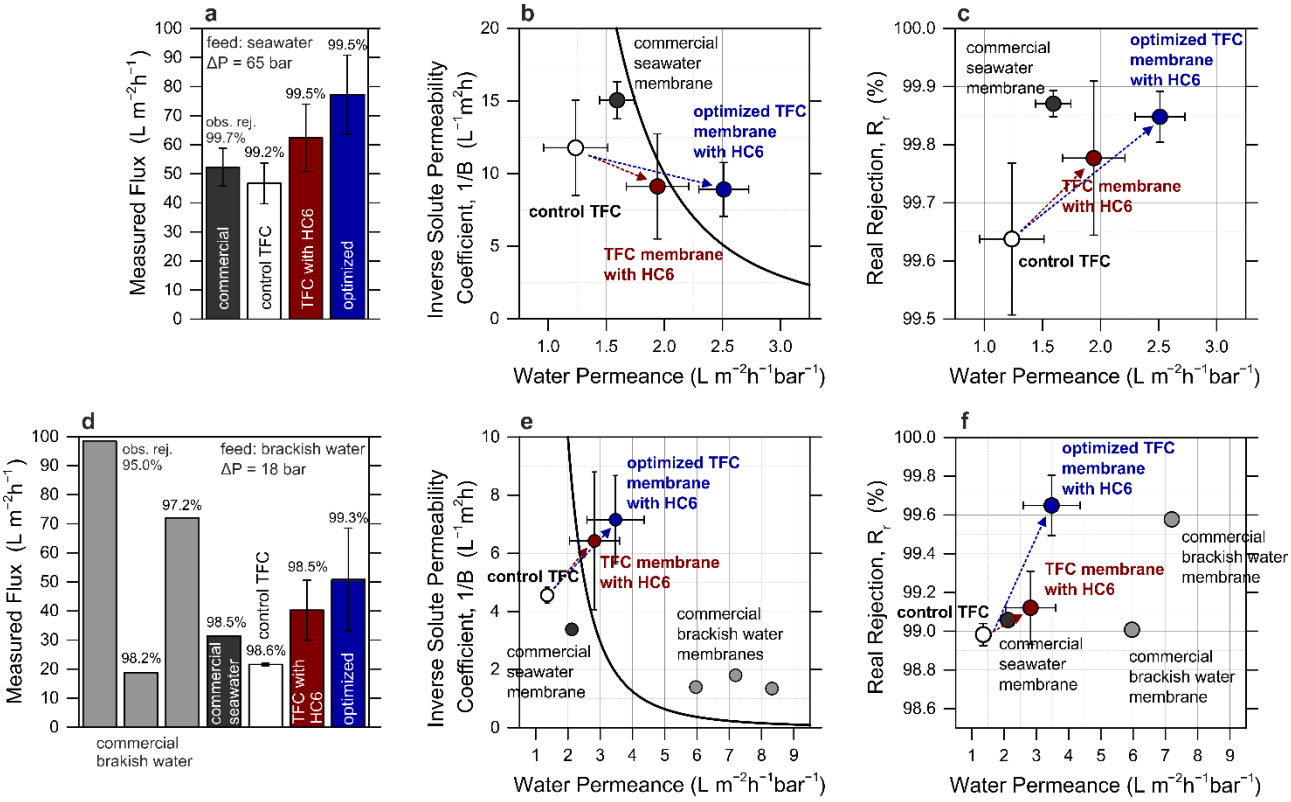

Fig. 3 | Performance of the membranes in the desalination of **(a-c)** seawater and **(d-f)** brackish water. (**a**, **d**) Experimental water flux and observed solute rejection of control TFC membranes, commercial membranes, and TFC-HC6 membranes incorporating AWCs at 0% recovery. The filtration conditions were: 65 bar applied pressure with 35000 ppm NaCl feed solution at pH 8 for seawater desalination; 18 bar applied pressure with 5800 ppm NaCl feed solution at pH 7 for brackish water desalination. **(b, e)** Selectivity-productivity trade-off graphs plotting the inverse solute permeability coefficient of the membranes as a function of their respective water permeance; the solid line depicts the proposed TFC upper bound relationship. (**c**, **f**) Calculated real rejection of the membranes as a function of respective water permeance. The feed solution temperature in all the tests was 27±1 °C.

This notable productivity was achieved while maintaining or, in many instances, while improving the observed NaCl solute rejection to ~ 99.5%, relative to traditional TFC membranes. The membranes proposed in this study also displayed a better combination of productivity and selectivity compared to marketed state-of-the-art membranes, which were tested in the lab under analogous conditions. Please note that an increase in the solute permeability coefficient *(B)* is commonly expected when the water permeance (*A*) increases, as *B* represents the flux of solutes dissolved in the permeating water: thus, as water flux increases, the solute flux is also higher at equivalent values of solute rejection. However, in this study, higher water permeance was obtained

with little increase, or even with a decrease of solute permeability coefficient. This phenomenon is explained with the concurrent increase of both water flux and solute rejection (Fig. 3b,c,e,f). A conventional and robust method to compare different membranes is to plot their performance in a permeability-selectivity trade-off chart (Fig. 3b,e). While the data associated with lab-made control membranes are placed below the upper bound, mostly due to a low water permeance, the membranes incorporating AWCs defeat the trade-off. This result is especially true for optimized TFC-HC6 membranes, whose permeability-selectivity performance places them well beyond the bound line. The improvements accomplished with the incorporation of AWCs are especially evident when the real rejection provided in desalination experiments is plotted against the water permeance (Fig. 3c,f). Real rejection is evaluated taking into account concentration polarization phenomena that occurred during filtrations and is a better parameter than observed rejection to understand the intrinsic selectivity of the membranes. To assess the performance of the bioinspired membranes with real seawater, low-recovery experiments were also performed using the recipe for substitute ocean water described in Table X1.1 of the ASTM D1141-98 (2013) as feed solution. A water flux of 66.8 ± 3.8 LMH was obtained, with an observed conductivity rejection of 99.4 ± 0.1 %, and an observed boron rejection of 91.2 ± 1.5%. Please see the Supporting Information for further details on the experimental conditions, on the ionic composition of the feed and permeate samples, as well as for values of observed rejection of individual ions.

The membranes TFC-HC6 incorporating AWCs were further assessed when applied in high-recovery filtration, as in commercial desalination processes. Experiments were conducted by achieving 50% recovery of freshwater from a synthetic feed approximating the salinity and the pH of typical seawater. The data in Fig. 4a,b, show the trend of permeate flux as a function of recovery: the flux profile decreases steadily from the initial value of 75 L m^{-2} h^{-1} due to the reduction in driving force as the feed solution was increasingly concentrated. The average water flux of the test was 34.4 L m^{-2} h^{-1} and the concentration of the product water was 290 mg/L, a value related to an

excellent palatability based on the WHO Guidelines for Drinking-Water Quality. This experiment approaches the flux profile and the solute concentrations that would be obtained inside a pressure vessel of a full-scale system for a single pass sweater RO process, and it confirms the promising transport performance of the TFC-HC6 membranes under representative full-scale conditions. We surmise that the enhanced fluid dynamics of real membrane elements would further reduce the effect of concentration polarization when compared with lab-scale experiments, thus realizing even larger water fluxes and a higher permeate quality.

Therefore, a vessel-scale model was implemented to compute the membrane area and the energy required to extract high-quality water from a feed of seawater, by applying current commercial RO membranes and the bioinspired membranes proposed in this work.

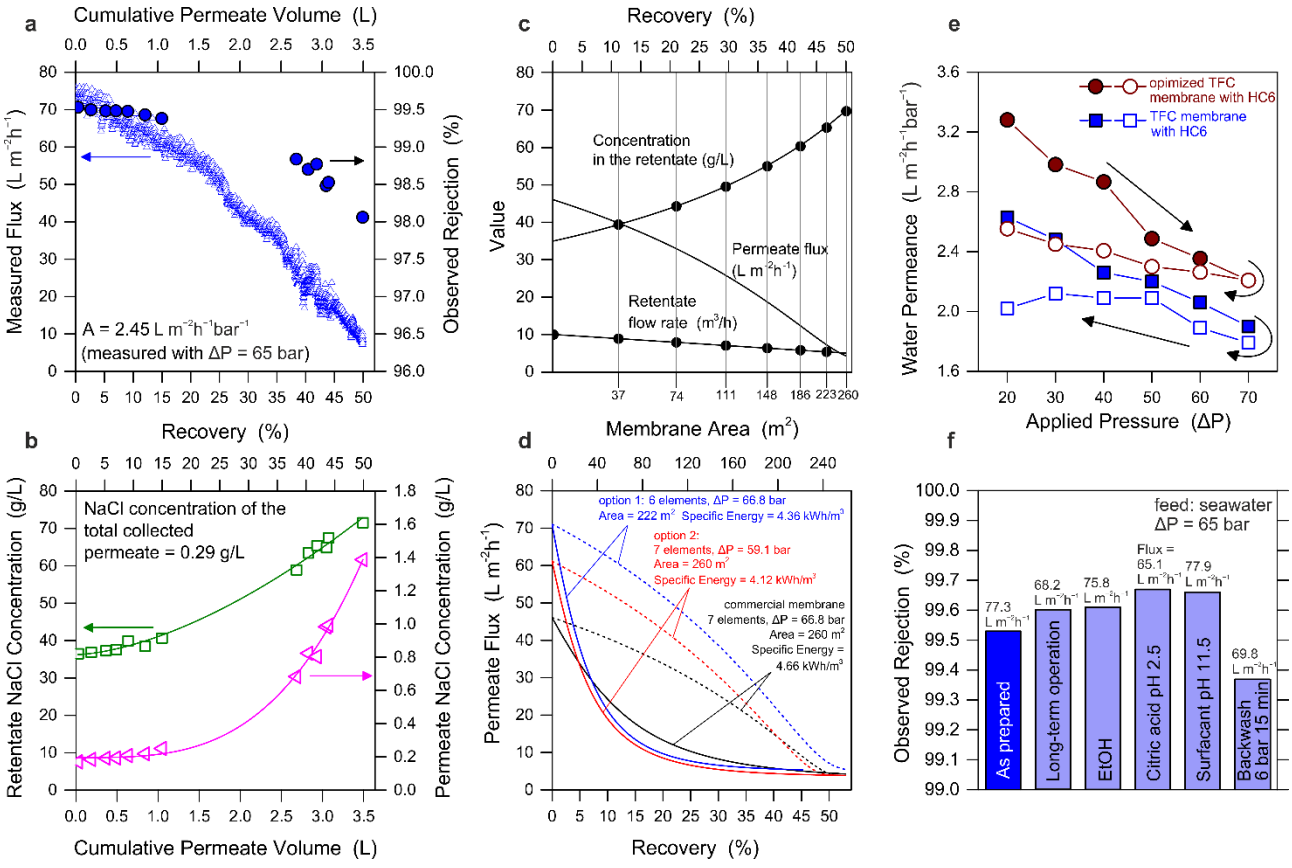

Fig. 4 | Application of the membranes in typical seawater desalination operation. (a, b) Experimental water flux, observed solute rejection, feed and permeate stream concentrations as a function of recovery and cumulative permeate volume; here, the filtration conditions were: 65 bar applied pressure with 35,000 ppm NaCl feed solution at pH 8 and a final recovery of 50%. **(c)** Validation of the vessel-scale model for SW30XHR commercial membranes and **(d)** outcome of the application of the model for the commercial membranes and for the TFC-HC6 membranes

incorporating AWCs; here, the profile of permeate flux within the vessel is plotted as a function of (solid lines) space, i.e., cumulative membrane area, or (dash lines) recovery rate. **(e)** Experimental water permeance in tests comprising a stepwise increase followed by a stepwise decrease of applied pressure. **(f)** Experimental performance of membranes subjected to mechanical or chemical stress; here, the filtration conditions were: 65 bar applied pressure with 35,000 ppm NaCl feed solution at pH 8 and recovery of 0%.

As shown in Fig. 4c, the vessel-scale model, represented by solid lines, was first validated with high-rejection SW30XHR-400i DuPont elements, against the results provided by the software Wave (DuPont) and plotted as black dots. The model accurately described the profile of flux and concentration within the system. Once validated, the model was thus applied in two optional implementations of our bioinspired membranes (Fig. 4d). The modeling outcome suggests that, if the same pressure of 66.8 bar is applied in the vessel, 50%-recovery desalination may be achieved with six instead of seven elements in series, which are instead needed when applying current commercial seawater desalination membranes. In other words, the larger permeance of the membrane TFC-HC6 incorporating AWCs would allow the use of a smaller membrane area, translating in near proportional savings in capital and membrane replacement costs, with also a reduction of the specific energy from 4.66 to 4.36 kWh for each m^3 of product freshwater. A possibly more advantageous configuration would involve the same number of elements with respect to current commercial membranes, that is, identical membrane area and capital costs, but a lower applied pressure of 59.1 bar. According to the model, this arrangement would provide a more uniform permeate flux within the vessel and a noteworthy 12% reduction of the required energy to produce the same amount of freshwater. It is important to highlight that the application of membrane elements is subject to several constraints in terms of minimum and maximum cross-flow rate, maximum permeate flux, as well as maximum recovery rate, which can only be evaluated at the time of full-scale system design.

A final set of experiments were conducted to understand the resilience of the layers to mechanical and chemical stress. The materials displayed a partially plastic behavior, as membranes could not

entirely recover their original permeance once subjected to high hydraulic pressures (Fig. 4e). Nevertheless, the novel membranes were notably robust and maintained their selectivity after being subject to mechanical solicitations, including changes in pressure, to backwash, and in long-term filtration experiments. The transport performance of the bioinspired membranes was also unaffected by exposure to relatively harsh environments representative of real systems, where membranes would undergo cycles of physical and chemical cleaning, often with the use of acidic, basic, and/or amphiphilic compounds. The results in Fig. 4f indicate that similar or higher NaCl rejection than pristine membranes was observed after these were exposed to solutions of different chemistry. Perhaps the most significant outcome is related to the ability of the materials to maintain high performance following immersion in pure ethanol, which was used during HC6 synthesis and to solubilize this compound during membrane fabrication. This result suggests that the AWCs were effectively incorporated within the PA matrix and no detrimental effects of leaching or re-solubilization were detected, as the membranes showed no loss in performances (Fig. 4f).

This rationalization corroborates the results discussed above, suggesting that the embedded self-assembled AWCs did not generate defects of the uppermost active layer. Indeed, the highly selective AWC are intrinsically promoting the preferential selective passage of water with a significantly better perm-selective behavior through a selective AWC embedded layer with larger surface area. It also implies an excellent structural compatibility of AWCs with the surrounding PA matrix, a necessary requisite to construct a seamless active layer without defects.

Supplementary Information is available in the online version of the paper.

Acknowledgements: This work was supported by Agence Nationale de la Recherche ANR-18-CE06-0004-02, WATERCHANNELS and ERANETMED2-72-357 IDEA. The authors thank Francesco Ricceri (Politecnico di Torino) for help with filtration experiments.

Author Contributions M.B. conceived the project. M.Di V. fabricated the membranes, performed IR, EDX characterization and SEM analysis; L. H. performed XPRD analysis, M.Di V. and A. T. designed and performed the filtration experiments. V.M. S.C. S. N. performed DLS, SAXS and

TEM experiments and conducted their experimental analysis. M.B. wrote the manuscript with input from all authors.

References

1. Mekonnen, M. M. & Hoekstra, A. Y. Four billion people facing severe water scarcity. *Sci. Adv.* **2,** e1500323–e1500323 (2016).
2. Eliasson, J. The rising pressure of global water shortages. *Nature* **517,** 6–7 (2015).
3. Shannon, M. A. *et al.* Science and technology for water purification in the coming decades. *Nature* **452**, 301–310 (2008).
4. Cadotte, J. E., Petersen, R. J., Larson, R. E. & Erickson, E. E. A new thin-film composite seawater reverse osmosis membrane. *Desalination* **32**, 25–31 (1980).
5. Karan, S., Jiang, Z. & Livingston, A. G. Sub-10 nm polyamide nanofilms with ultrafast solvent transport for molecular separation. *Science (80-.).* **348**, 1347–1351 (2015).
6. Chowdhury, M. R., Steffes, J., Huey, B. D. & McCutcheon, J. R. 3D printed polyamide membranes for desalination. *Science (80-.).* **361**, 682–686 (2018).
7. Tan, Z., Chen, S., Peng, X., Zhang, L. & Gao, C. Polyamide membranes with nanoscale Turing structures for water purification. *Science (80-.).* **360**, 518–521 (2018).
8. Jeong, B. H. *et al.* Interfacial polymerization of thin film nanocomposites: A new concept for reverse osmosis membranes. *J. Memb. Sci.* **294**, 1–7 (2007).
9. Duan, J. *et al.* High-performance polyamide thin-film-nanocomposite reverse osmosis membranes containing hydrophobic zeolitic imidazolate framework-8. *J. Memb. Sci.* **476**, 303–310 (2015).
10. Ratto, T. V, Holt, J. K. & Szmodis, A. W. Asymmetric nanotube containing membranes. *U.S. Pat. Appl. Publ.* 6 pp., Chemical Indexing Equivalent to 155:485735 (2011).
11. Werber, J. R., Deshmukh, A. & Elimelech, M. The Critical Need for Increased Selectivity, Not Increased Water Permeability, for Desalination Membranes. *Environmental Science and Technology Letters* **3**, 112–120 (2016).
12. Agre, P. Aquaporin water channels (nobel lecture). *Angewandte Chemie - International Edition* **43**, 4278–4290 (2004).

13. Eriksson, U. K. *et al.* Subangstrom resolution x-ray structure details aquaporin-water interactions. *Science (80-.).* **340**, 1346–1349 (2013).

14. Tang, C. Y., Zhao, Y., Wang, R., Hélix-Nielsen, C. & Fane, A. G. Desalination by biomimetic aquaporin membranes: Review of status and prospects. *Desalination* **308**, 34–40 (2013).

15. Barboiu, M. Artificial water channels. *Angew. Chemie - Int. Ed.* **51**, 11674–11676 (2012).

16. Barboiu, M. & Gilles, A. From natural to bioassisted and biomimetic artificial water channel systems. *Acc. Chem. Res.* **46**, 2814–2823 (2013).

17. Leduc, Y. *et al.* Imidazole-quartet water and proton dipolar channels. *Angew. Chemie - Int. Ed.* **50**, 11366–11372 (2011).

18. Hu, X. B., Chen, Z., Tang, G., Hou, J. L. & Li, Z. T. Single-molecular artificial transmembrane water channels. *J. Am. Chem. Soc.* **134**, 8384–8387 (2012).

19. Si, W. *et al.* Selective artificial transmembrane channels for protons by formation of water wires. *Angew. Chemie - Int. Ed.* **50**, 12564–12568 (2011).

20. Licsandru, E. *et al.* Salt-Excluding Artificial Water Channels Exhibiting Enhanced Dipolar Water and Proton Translocation. *J. Am. Chem. Soc.* **138**, 5403–5409 (2016).

21. Tunuguntla, R. H. *et al.* Enhanced water permeability and tunable ion selectivity in subnanometer carbon nanotube porins. *Science (80-.).* **357**, 792–796 (2017).

22. Kocsis, I. *et al.* Oriented chiral water wires in artificial transmembrane channels. *Sci. Adv.* **4**, (2018).

23. Werber, J. R. & Elimelech, M. Permselectivity limits of biomimetic desalination membranes. *Sci. Adv.* **4**, (2018).

24. McGinnis, R. L. *et al.* Large-scale polymeric carbon nanotube membranes with sub-1.27-nm pores. *Sci. Adv.* **4**, (2018).

25. Mi, B. Graphene oxide membranes for ionic and molecular sieving. *Science* **343**, 740–742 (2014).

26. Yang, Y. *et al.* Large-area graphene-nanomesh/ carbon-nanotube hybrid membranes for ionic and molecular nanofiltration. *Science (80-.).* **364**, 1057–1062 (2019).

27. Shen, Y. X. *et al.* Achieving high permeability and enhanced selectivity for Angstrom-scale separations using artificial water channel membranes. *Nat. Commun.* **9**, (2018).

28. Lin, L., Lopez, R., Ramon, G. Z. & Coronell, O. Investigating the void structure of the polyamide active layers of thin-film composite membranes. *J. Memb. Sci.* **497**, 365–376 (2016).

29. Pacheco, F., Sougrat, R., Reinhard, M., Leckie, J. O. & Pinnau, I. 3D visualization of the internal nanostructure of polyamide thin films in RO membranes. *J. Memb. Sci.* **501**, 33–44 (2016).

30. Wong, M. C. Y., Lin, L., Coronell, O., Hoek, E. M. V. & Ramon, G. Z. Impact of liquid-filled voids within the active layer on transport through thin-film composite membranes. *J. Memb. Sci.* **500**, 124–135 (2016).

31. Li, Y. *et al.* Probing flow activity in polyamide layer of reverse osmosis membrane with nanoparticle tracers. *J. Memb. Sci.* **534**, 9–17 (2017).